ORIGINAL ARTICLE

Powder stream thermal dynamics in directed energy deposition for high aggregation and thermal efficiency using computational fluid dynamics modeling

Xiaoguang Qu[1] · Ze Chai[2] · Tongtong Liu[1] · Huabin Chen[1] · Xiaoqi Chen[1,3]

Abstract

Exactly converging the metal powder flux at a given substrate position is of great importance for additively manufacturing high-quality metallic products, and it essentially depends on the geometric structure and thermal dynamics of powder streams. In this study, we developed a 3D numerical model to elucidate the interactions between powder, gas, and laser beam in a coaxial nozzle during laser directed energy deposition (DED). The numerical simulation indicates that the waist-shaped powder stream converges approximately 11.2 mm below the nozzle outlet, where the minimum nominal radius is achieved. Within the laser irradiation area, the powder particle temperature increases dramatically and reaches the maximum average value at approximately 20 mm away from the nozzle outlet. Furthermore, optimal powder stream convergence and high thermal efficiency can be achieved when the powder stream driven by low inner gas flow rate converges 4 mm below the laser beam focal plane. The results of high-speed and infrared imaging analysis demonstrate that the proposed model has good predictability for the mean particle velocity and temperature, with average R^2 of 0.91 and 0.96, respectively. This study provides an effective approach to achieve desired metal-powder stream convergence and high thermal efficiency for DED powder feeding.

Keywords Directed energy deposition · Computational fluid dynamics · Powder stream structure · Powder stream consolidation · Thermodynamics

1 Introduction

Over the last two decades, the additive manufacturing (AM) technique has evolved rapidly from scientific research to industrial production [1–3]. As one of the most representative laser AM methods, direct energy deposition (DED) delivers a feedstock material in the form of metal powder or wire to the processing area accompanied by a coaxial laser beam to heat the feedstock and substrate material, while metal deposition assembly moves layer by layer with the CNC-controlled robot motion [4–7]. Such a mechanical configuration makes the DED process highly flexible and versatile, and compared with the traditional manufacturing means, the near net shape DED manufacturing of metal parts is considered to be cost-effective and highly efficient [8–10]. With the state-of-the-art technique, a wide variety of metal materials, such as hard-to-process superalloys, high-performance aluminum alloys, and complex-shaped titanium alloy parts, have been successfully manufactured and applied in many industrial fields [11, 12].

Powder-based DED has a wide range of applications due to its high precision and design freedom. In the primary stage of DED, the metal particles supplied by the powder feeder are blown out of the nozzle by a high-speed inert gas. After leaving the nozzle, powder particles can absorb heat from the interaction with the laser beam, while dissipating part of the heat via convection and radiation.

✉ Ze Chai
chaize@sinap.ac.cn

✉ Xiaoqi Chen
xqc@scut.edu.cn

1 Shanghai Key Laboratory of Materials Laser Processing and Modification, School of Material Science and Engineering, Shanghai Jiao Tong University, Shanghai 200240, People's Republic of China

2 Shanghai Institute of Applied Physics, Chinese Academy of Sciences, Shanghai 201800, People's Republic of China

3 Wu Shien-Ming School of Intelligent Engineering, South China University of Technology, Guangzhou 511442, People's Republic of China

During flight, some particles even melt and evaporate. Ultimately, all powders reach the deposition area but only part of them are captured and transfer mass and heat to the molten pool to form the cladding. The powder feeding process is very complex that significantly affects the cladding formation [13, 14]. Therefore, the interactions between the powders, gas, and laser beam during DED are of great significance for both the deposition efficiency and deposited workpiece quality.

A large number of experimental and theoretical researches have been conducted to investigate the powder flow process in laser DED. Some use statistical methods to develop relevant analytical models to predict the powder distribution. Mouchard et al. [15] employed an analytical model to reproduce the powder flow distribution from a coaxial annular nozzle to the powder focus position, characterizing the concentration of powder stream as a discrete sum of Gaussian distributions. By considering the powder flow as separate Gaussian distributions, Liu et al. [16] created an analytical model in which the simple arithmetic average of the powder flow from four-jet nozzles is calculated as the total concentration distribution. With a Gaussian distribution directly used to quickly determine the powder concentration variations, Pinkerton and Li [17, 18] proposed an analytical approach considering the powder flow as two separate cases before and after convergence point. Besides powder concentration, Tan et al. [19] developed an analytical method to characterize the temperature evolution of incident particles under different laser power and incident angles, based on image gray analysis. The analytical method analyzes a large amount of statistical data based on the priori assumption of Gaussian distribution which performs optimally within the Gaussian region. However, the distribution of the powder stream from the nozzle outlet to the substrate does not always follow a Gaussian pattern. And particles cannot be clearly recorded due to small size, high velocities, and opaque nozzle. Moreover, analytical models overlook the physical essence of certain complex phenomena, such as the interaction between powder and gas, and particle heating and melting during the powder feeding process [20].

Due to the limitations aforementioned, computational fluid dynamics (CFD) combined with experimental validation has been widely employed to build physical models about powder flow. Gao et al. [21] utilized CFD and discrete element methods to simulate the interactions between the powder particles and gas flows, in which the predefined laser irradiation rate and powder aggregation degree were used to assess the impact of nozzle geometries on powder flow. Pacheco and Cardoso [22] concentrated on the thermomechanical behavior of discrete particles interacting with a laser source. They discussed the effects of variations in laser power, initial velocity, and surface energy on the powder flow bonding process. Zhang et al. [23] adopted a k-ε based gas–solid two-phase flow theory to simulate the powder flow field and a separate model was developed in FLUENT to evaluate the powder concentration. Wen et al. [24] presented a 2D axis symmetrical numerical model to predict the coaxial powder flow. The thermodynamic behavior of multi-particles is completely modeled by solving the coupled momentum transfer equations between the particle and gas phase. Guan and Zhao [25] developed a numerical model for powder stream dynamics, incorporating laser attenuation and two-way coupling between gas and particles. Reynolds averaged Navier–Stokes (RANS) was chosen to solve the turbulent continuum gas flow, while a discrete phase model (DPM) was applied to describe the powder dynamic behavior. Tabernero et al. [26] proposed a turbulence k-ε based numerical model to simulate the powder flux distribution in which the energy density attenuation was estimated.

The previously mentioned numerical simulation extensively used the k-ε method for gas turbulence modeling. Actually, the k-ε model excels in fully developed turbulence but is not well-suited for the DED powder feeding process. Numerous studies [27, 28] have proved that the k-ω model outperforms k-ε in powder feeding process, due to its capability for addressing the low Reynolds number turbulence and near wall internal flow. Furthermore, there are no normalized metric features to quantitatively characterize the concentration distribution of the powder stream. How to achieve a powder stream with improved convergence and thermal efficiency also remains underexplored. To bridge this gap, we proposed a systematic approach to investigate the thermal dynamics of the powder stream in DED using CFD modeling.

In this study, a three-dimensional two-phase flow numerical model was developed to investigate the complex thermodynamic behavior of the powder feeding process which considers the particle size, powder-gas interaction, laser irradiation, and beam divergence. A more comprehensive k-ω model was utilized to solve the low Reynolds number turbulence of the gas phase. High-speed imaging and infrared camera observations were also carried out to validate the theoretical model. Moreover, based on two-phase flow simulation, the matching relationship between the powder flow and the laser beam was discussed to achieve a higher thermal efficiency which is commonly difficult to be determined experimentally. The theoretical powder heating efficiency shows a clear improvement from 39.7 to 55.9%. The proposed method provides an effective way for enhancing the convergence and thermal efficiency of the DED powder stream, and the simulation prediction can be used to further build the high-fidelity model of the entire DED process.

2 Methodology

The CFD numerical modeling of powder feeding process is described in Sects. 2.1 and 2.2. Experimental validation is described in Sects. 2.3 and 2.4.

2.1 Numerical modeling of powder feeding

The powder gas flow is considered as a dispersed multiphase flow, which regards the gas and the powder as the continuous phase and discrete phase, respectively. In this paper, the Euler–Lagrange [29] method is utilized to model the gas-powder flow. A one-way coupling strategy is used to solve the momentum transfer between these two phases due to the small powder size with dilution fraction less than 10% in gas. To save computational costs, while maintaining the representability of simulation, some appropriate assumptions are made as follows:

(1) The continuous gas phase is in a steady state, as the incompressible Newtonian fluid.
(2) All powder particles are spherical, and the particle diameter conforms to a Gaussian distribution with a mean diameter of 80 μm and a variance of 10 μm.
(3) The interaction between the powder particles and nozzle walls is completely elastic.
(4) The model only accounts for gravity, drag force, and inertia.
(5) The laser beam intensity conforms to a Gaussian distribution.
(6) The evaporation and radiative heat dissipation from particles are neglected.
(7) The temperature inside the particle is uniform.

2.1.1 Gas flow governing equations

The continuous gas flow can be described by the incompressible, Newtonian continuity equation and the momentum conservation equation in fluid mechanics. Also called the Navier–Stokes (NS) equation as follows:

Conservation equation of mass:

$$\nabla \cdot \mathbf{u} = 0 \tag{1}$$

Conservation equation of momentum:

$$\frac{\partial \rho u}{\partial t} + \nabla \cdot (\rho uu) = -\nabla p + \nabla \cdot \tau + \rho g \tag{2}$$

$$\tau = \mu(\nabla u + \nabla u^T) - \frac{2}{3}\mu I(\nabla \cdot u) \tag{3}$$

where the bold formatted quantities represent vectors; ρ is the density of the gas phase which is a constant due to the low Mach number and relatively low pressure drop. ∇ is the Hamiltonian; t and p are the time and pressure, respectively; $\mathbf{u}$ is the velocity vector; $\mathbf{g}$ is the gravitational acceleration of 9.8 m/s²; τ is the viscous stress tensor described by Eq. (3), in which μ is the dynamic viscosity. The flow state of a fluid is determined by the Reynolds number and defined as:

$$\text{Re} = \frac{\rho u L}{\mu} \tag{4}$$

In Eq. (4), the *Re* of the nozzle gas flow can be estimated to be approximately 4056, the gas density ρ is 1.634 kg/m³, the averaged gas velocity is 4 m/s, the nozzle exit diameter is 14 mm, and the dynamic viscosity is obtained as 22.56 μPa•s. The calculated *Re* is higher than the critical value of 2300, indicating the dominance of inertial effects over the viscous effects in gas flow. Therefore, the velocity oscillations and violent mixed transport phenomena in the continuous phase flow will occur, making the solution of the pure NS equation computationally intensive.

To accurately and effectively model the DED gas flow turbulence, the RANS approach is usually applied to decompose the flow to the average and fluctuating component. The Boussinesq eddy viscosity approximation [28] computed the Reynolds stress tensor as follows:

$$-\rho\overline{\mathbf{u}\,'\mathbf{u}'} = \mu_T(\nabla\overline{\mathbf{u}} + \nabla\overline{\mathbf{u}}^T) \tag{5}$$

where $\mathbf{u}'$ is the corresponding pulsation velocity; $\bar{\mathbf{u}}$ is the averaged velocity; μ_T represents the eddy viscosity which needs to be modeled further. In this study, the *k-ω* turbulence model [30] is selected due to its better performance and compatibility for wall bounded and low-*Re* turbulence of coaxial nozzle gas flow. The *k-ω* model is capable to transform the pulsating velocity into an instantaneous average velocity by solving the transport equations for turbulence kinetic energy (*k*) and energy dissipation rate (*ω*). The detailed information can be seen in Ref. [31].

2.1.2 Powder flow governing equations

As mentioned above, the momentum transfer between the gas and particles is described in terms of one-way coupling strategy. The trajectory, velocity, and forces of the particles are solved using the COMSOL [32] particle tracking interface in which the drag force, gravity, particle collisions, and inertial forces are taken into account for particle dynamics. The governing equations of the powder particle dynamics are given as follows:

$$\frac{d\mathbf{v}}{dt} = \frac{1}{\tau_p}(\mathbf{u} - \mathbf{v}) + \frac{\rho_p - \rho}{\rho_p}\mathbf{g} + \frac{4E}{3(1 - pois^2)}\sqrt{\frac{d_p\delta^3}{2}} \tag{6}$$

$$\tau_p = \frac{4\rho_p d_p^2}{3\mu C_D Re_r} \tag{7}$$

where the bold formatted quantities represent vectors; *u* and *v* are the velocity vectors; the second term on the right-hand side of Eq. (6) is the particle gravity which considers the effect of buoyancy, while the first term describes the drag force to obtain the turbulence effect on particles. And the third term is the particle collision forces based on classical Hertz theory [33] where E is Young's modulus, *pois* is Poisson's ratio, and δ is the particle deformation. τ_p is the velocity response time, which needs to be further modeled according to the relative Reynolds number Re_r:

$$Re_r = \frac{\rho|u - v|d_p}{\mu} \tag{8}$$

The particle shapes are not all perfectly spherical in DED, thus the Haider-Levenspiel [34] drag coefficient was used by considering the sphericity of the particles. This coefficient is given by:

$$C_D = \frac{24}{Re_r}(1 + A * Re_r{}^B) + \frac{C}{1 + D/Re_r} \tag{9}$$

where *A*, *B*, *C*, and *D* are all dimensionless empirical correlations of the particle sphericity defined as follows:

$A = \exp(2.3288 - 6.4581S + 2.4486S^2)$
$B = 0.0964 + 0.5565S$
$C = \exp(4.905 - 13.8944S + 18.4222S^2 - 10.2599S^3)$
$D = \exp(1.4681 + 12.2584S - 20.7322S^2 + 15.8855S^3)$

In this study, the sphericity *S* is set to be 0.5, which defines the surface ratio of a volume equivalent sphere to the considered non-spherical particle.

Besides, the turbulence diffusion by instantaneous flow fluctuations is the main mechanism for particle dispersion and deposition. Hence, a stochastic discrete random walk (DRW) [35] approach is used to describe the particles turbulent dispersion in which the drag force is computed by first adding a random velocity perturbation to the mean flow field based on the local value of the kinetic energy *k*.

To characterize the convergence of the powder stream, a user-defined function is chosen to calculate the concentration distribution of particles from the Lagrange trajectory using the particle source in cell (*PSI-C*) [36]:

$$C_j = \frac{\dot{M}\sum_{i=1}^n dt_{(i,j)}}{V_j} \tag{10}$$

where $\dot{M}$ is the number flow rate of each trajectory, V_j is the volume of a computational cell, *dt* is the particle residence time, and the subscript (*i,j*) refers to the *i*th trajectory and the *j*th cell.

2.1.3 Powder heating

Additionally, the particles are heated by laser irradiation during flight and even undergo phase changes such as melting, while dissipating heat in the forms of convection and radiation. During the flight of particles, the energy conversation equations are given as follows:

$$m_p C_p \frac{\partial T}{\partial t} = \alpha I A_p - hS_p(T - T_0) - m_p L\frac{df_l}{dt} \tag{11}$$

where m_p is the particle mass; C_p is the specific heat of powder particle; *T* and T_0 are the temperatures of particles and gas environment, respectively; α is the laser absorption coefficient of particles; *I* is the laser intensity; A_p is the effective irradiated area of powder particles on laser beam; S_p is the surface area of powder particle; *h* is the convective heat transfer coefficient; *L* is the latent heat of fusion; and f_l is the liquid phase fraction.

The dimensionless number *Bi* describes the distribution pattern of the temperature field inside an object under non-stationary thermal conductivity, which is defined as:

$$Bi = \frac{h}{k_p}L_C \tag{12}$$

where L_c is the characteristic length, typically the ratio of particle volume to surface area, and k_p is the thermal conductivity. Note that the temperature inside the particle can be assumed as uniform and calculated as a single number rather than a temperature distribution due to a small value of *Bi*. The convective heat transfer coefficient *h* is specified by the Nusselt number (*Nu*) [37], which is written as:

$$Nu = \frac{hd_p}{k_g}2 + 0.6Re^{0.5}Pr^{0.33} \tag{13}$$

where k_g is the thermal conductivity of gas; *Pr* is the Prandtl number, written as:

$$Pr = \frac{C_{p,g}\mu}{k_g} \tag{14}$$

where $C_{p,g}$ is the specific heat of gas.

Some particles may undergo phase transitions under laser irradiation during flight. To accurately model the temperature evolution of particles, the liquid fraction method is utilized to describe the phase change heat transfer. Such method adds the latent heat of phase transition as a source term into Eq. (11). A linear function is used to describe

the relationship between the liquid fraction f_l and particle temperature T:

$$f_l(T) = \begin{cases} 0, & T < T_s \\ \frac{T-T_s}{T_l-T_s}, & T_s \leq T \leq T_l \\ 1, & T > T_l \end{cases} \qquad (15)$$

where T_s and T_l are the solidus and liquidus temperatures, respectively. The derivative of f_l with respect to the time t can be expressed as:

$$\frac{df_l}{dt} = \begin{cases} 0 & T < T_s, T > T_l \\ \frac{1}{T_l-T_s}\frac{dT}{dt} & T_s < T < T_l \end{cases} \qquad (16)$$

The intensity of laser beam conforms to a Gaussian distribution at the focal plane and the planes which are parallel to the focal plane. It can be calculated from Eq. (17):

$$I = \frac{3P}{\pi R_b^2(z)}\exp(-\frac{3(x^2+y^2)}{R_b^2(z)}) \qquad (17)$$

where P is the laser power, and x and y are the Cartesian coordinates. In general, the convergence and divergence of the laser beam have a crucial effect on the powder stream heating efficiency. Hence, the laser beam effective radius $R_b(z)$ is considered as a piecewise function with respect to z. In this study, the laser beam with a radius of 1 mm at the focal plane is firstly focused at $z = -9$ mm with a half-angle $\varphi = 3.6°$, followed by a depth of field (DOF) of 4 mm, and then diverged with an identical half-angle. $R_b(z)$ can be calculated by Eq. (18):

$$R_b(z) = \begin{cases} (z+9)*\tan(\varphi)+1 & z \in (-9, +\infty) \\ 1 & z \in [-13, -9] \\ (-13-z)*\tan(\varphi)+1 & z \in (-\infty, -13) \end{cases} \qquad (18)$$

The calculated laser beam intensity profile is depicted in Fig. 1, where the intensity distributes more reasonably than that produced by using a conventional heat source.

2.2 Boundary conditions

A symmetrical 3D numerical model of the powder feeding process with annular nozzle is developed through COMSOL [32] software. The 3D geometry of the model and some of the boundary conditions are shown in Fig. 2a. The nozzle consists of an inner wall and an outer wall with two inlet planes, which are the transport channels of the carrier gas, powder, and protective gas. To investigate the kinetic behavior of the powder flow below the nozzle, a sufficiently large cylindrical free space is provided. Only half of the model is calculated to save computational cost due to the geometric
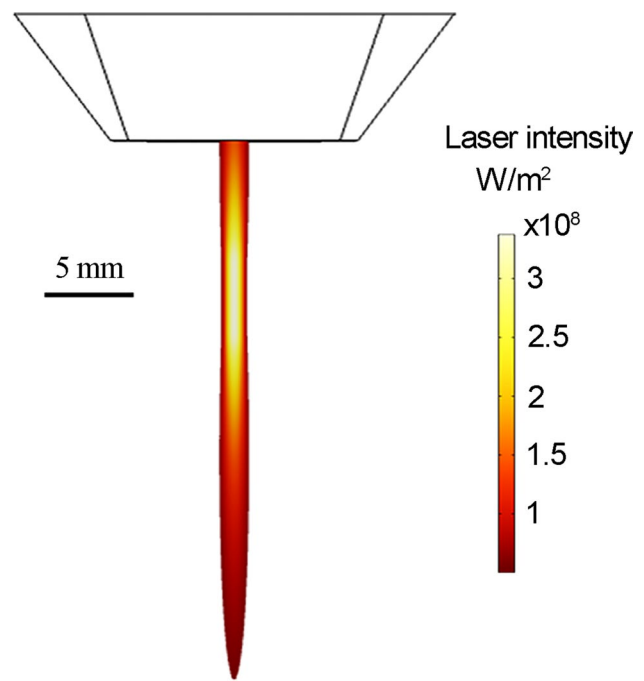

Fig. 1 Laser beam intensity profile with a radius of 1 mm at the focal plane, a half-angle of 3.6°, and a laser power of 800 W

symmetry of the nozzle. The corresponding boundary conditions are summarized as follows:

(1) Set velocity inlet and fully developed boundary conditions on both inlet planes according to the corresponding gas volume flow rates.
(2) Set non-slip boundary conditions on the nozzle walls.
(3) Pressure exit boundary conditions are set on the exit planes.
(4) Set a symmetry boundary condition on the symmetry plane.

The detailed input parameters of the boundary conditions and material physical properties are shown in Tables 1 and 2, respectively. About 5000 powder particles are randomly released from the inlet plane to fully investigate the particle movement and powder stream concentration.

To accurately and efficiently capture the flow field, temperature field, and powder concentration distribution, a high-quality 3D structured tetrahedral mesh is generated, and the nozzle walls and the z-axial parallel region are appropriately local refined. Totally 130,000 cells with a minimum cell mass of 0.1682 are generated and presented in Fig. 2b.

2.3 Powder feeding experiment setup

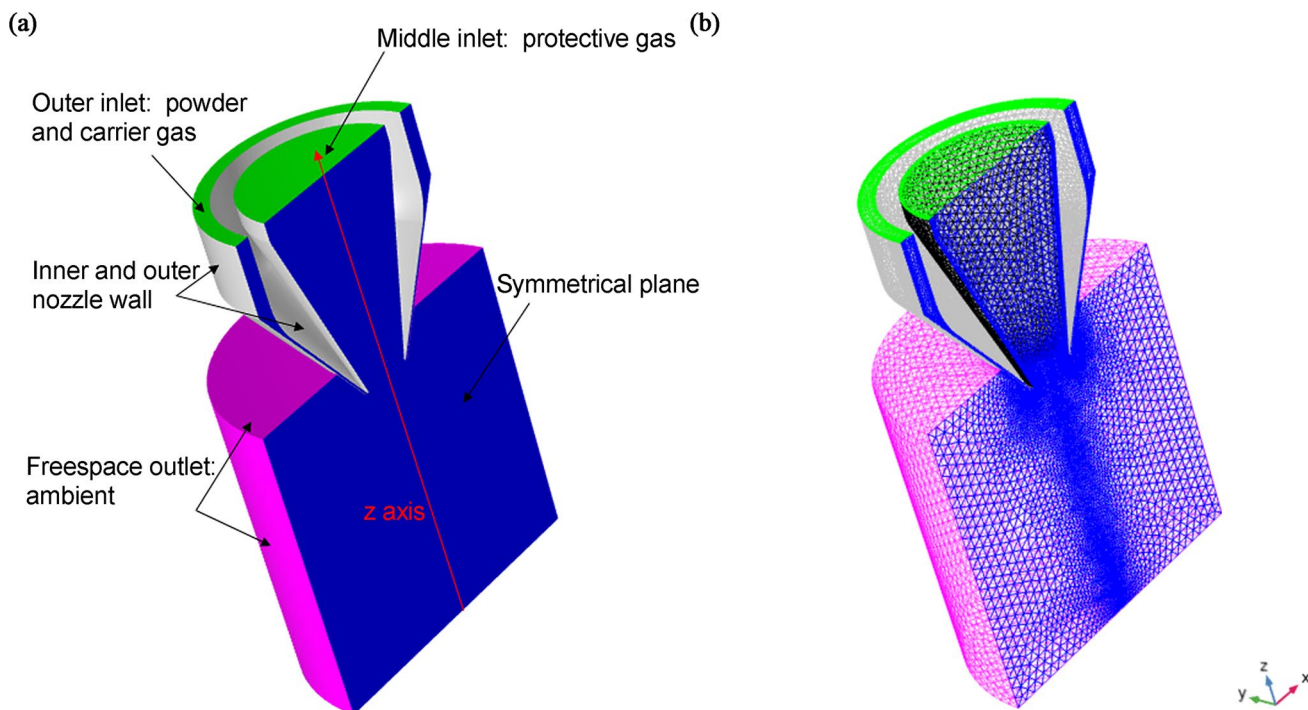In this study, a powder delivery observation experiment was set up for model validation. Commercially

Fig. 2 Modeling set-up: **a** geometry and boundary conditions and **b** mesh of the computational domain

Table 1 Boundary conditions for the simulation of DED powder feeding in coaxial nozzle

Boundary planes	Boundary conditions
Carrier gas inlet	Gas flow rate: 6, 8, 10 L/min
Protective gas inlet	Gas flow rate: 10, 15 L/min
Particles inlet	Powder flow rate: 6.54 g/min
Outlet	Pressure (relative): 0 Pa

Table 2 Thermo-physical properties of Inconel 718 and argon used in the simulation

Physical properties	Inconel 718 powder	Argon gas
Density	8190 (kg/m^3)	1.603 (kg/m^3)
Specific heat	600 (J/(kg•K))	520.6 (J/(kg•K))
Thermal conductivity	N/A	0.0158 (W/(m•K))
Latent heat	227 (kJ/kg)	N/A
Viscosity	N/A	22.5 (μPa•s)
Solidus	1528 (K)	N/A
Liquidus	1610 (K)	N/A
Emissivity	0.445	N/A
Absorption coefficient	0.2	N/A

gas-atomized Inconel 718 powders were used as the feeding materials whose stated diameter is within the range from 53 to 150 μm. The particles are spherically shaped with the size of D10 = 49.1 μm, D50 = 73.5 μm, and D90 = 124.5 μm according to actual measurement. The chemical compositions of Inconel 718 powders are shown in Table 3. Prior to experiments, the Inconel 718 powders were dried in a vacuum oven at 150 ± 10 °C for 2 h.

To systematically observe the thermal dynamic behavior of the powder flow, a high-speed imaging experiment system was established to record the powder stream in coaxial nozzle. As shown in Fig. 3, the DED experimental system used in this study is built around a 2000-W fiber laser (IPG, YLS-2000-CT) with a wavelength of 1070 nm as the heat source. The designed DED paths were performed by a 6-axis robot (KUKA, KR30HA). A coaxial nozzle (PRECITIEC, YC52) and a powder feeder with three hoppers (RAYCHAM, RC-PGF-D) were used for powder delivery as it has high conveying efficiency and uniformity. Argon gas of 99.99% high-purity was utilized to deliver metal powders and provide a protective atmosphere.

Besides, a high-speed camera (Photron FASTCAM SA-X2) with a 200-mm fixed-focus macro lens was used
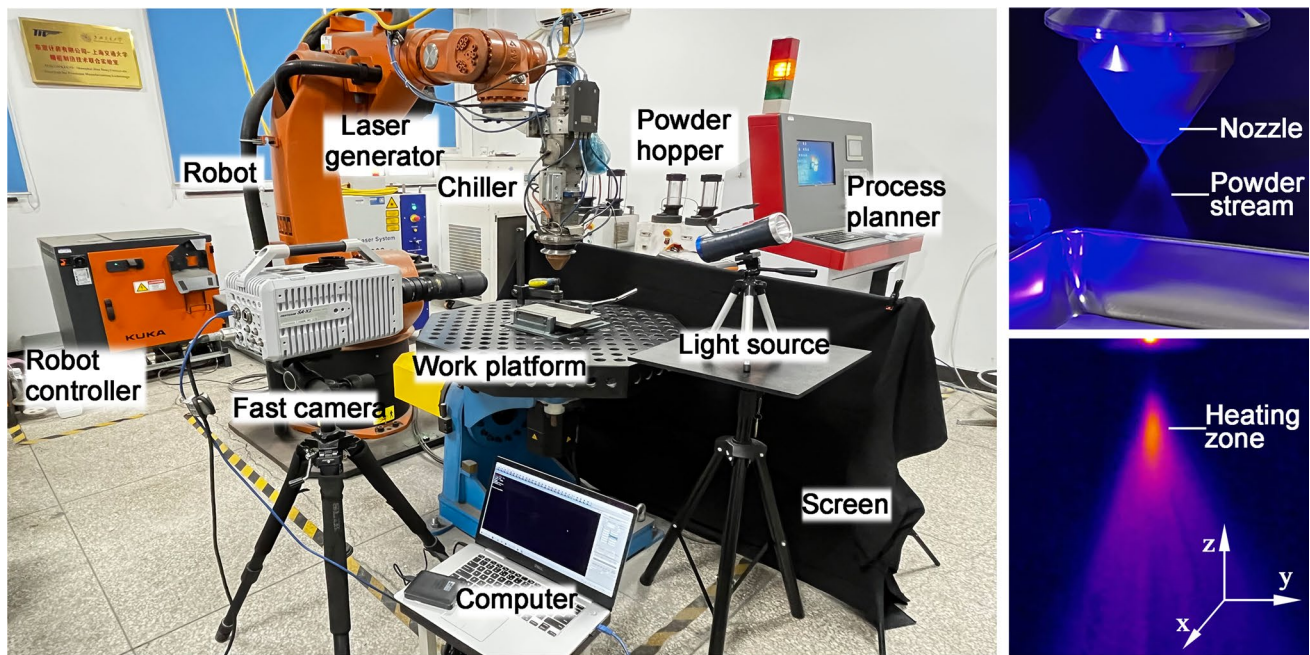
Table 3 The chemical compositions of Inconel 718 powders (wt%)

Elements	Cr	Fe	Nb	Mo	Al	Ti	Mn	Si	C	Ni
Contents	19.18	17.41	5.07	3.10	0.63	0.94	0.01	0.20	0.04	Bal

Fig. 3 Schematic of powder stream observation experiment

Table 4 Parameters of the high-speed camera used in this study

Resolution	Full resolution	Recording rate	Dynamic range	Exposure time
1024 × 1024	1000 fps	1 GB/s	10 bits	300 ns ~ 5 s

to capture the images and videos of the powder stream. During the powder feeding experiment, the high-speed camera was placed along the x-axis with the focal point located approximately in the powder convergence region to keep the powder stream in the center field of view. The axis of the nozzle is perpendicular to the XOY horizontal plane and a uniform blue light source illuminates the powder stream along the y-axis. Meanwhile, a dark screen was placed opposite to the camera to make powder stream more visible. The camera parameters are shown in Table 4. Furthermore, an infrared camera (InfRec NS9500, temperature measurement range 0–2000 °C) was used to detect the powder stream temperature.

To validate the numerical model, four levels of flow rates 8, 10, 12, and 15 L/min were chosen for the carrier gas and protective gas to fully investigate the effect of gas flow rates on the powder stream convergence. The powder feeding rate was fixed at 6.54 g/min which equivalents to 1 r/min of the powder feeder rotation speed. The laser beam has a radius of 1 mm, a half angle of 3.6°, and a focal length of 9 mm. The laser power was set from 600 to 1200 W in steps of 200

W for this study. During the photography, the powder feeding process was photographed for 1 s at a shutter speed of 0.001 s once it already reached a steady state.

2.4 Image processing-based powder stream measurement

The clear and sharp images are captured by the high-speed camera in powder feeding experiment. Image processing-based methods were used to characterize the powder stream convergence and concentration distribution. According to the Mie theory [38], the powder stream concentration is proportional to the gray value of the image under constant powder feeding parameters and photography conditions. To reduce the effect of background impurities and light source inhomogeneities, the acquired powder stream images are treated by the background correction using Eq. (19), where I is the original image, B is the background image without powder feeding, and I' is the preprocessed image.

$$I'(i,j) = I(i,j) - B(i,j) \tag{19}$$

In addition, the highly random and discrete distribution of powder particles in the original image is not accurate for analyzing the powder stream convergence. Thus, the random particle trajectories are considered as probability distributions, which will reach a steady state after a long enough time. In this study, nearly 500 consecutive

images are averaged to weaken the random effect of particle trajectories.

Moreover, the powder cluster nominal radius R_p is defined to characterize the powder stream aggregation. And p is the ratio of the powder amount within the effective central area to the whole powder spot, and it ranges from 0 to 1. A smaller R_p means the better powder stream convergence when p is constant. As shown in Fig. 4, the powder stream concentration distribution on a x–y horizontal section is divided into V_0 and V_1 by the red grid. Here, the volume V_0 represents the quantity of powder within the effective central area. Thus, the ratio p can be expressed as:

$$p = \frac{V_0}{V_1 + V_0} = \frac{\int_0^{R_p} 2\pi\rho(r)dr}{\int_0^{+\infty} 2\pi\rho(r)dr} \tag{20}$$
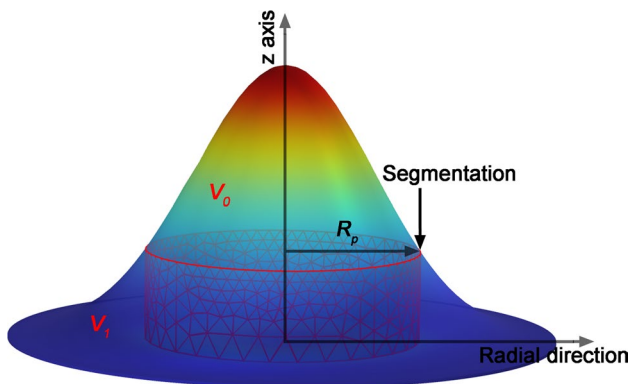
Fig. 4 Schematic of defining nominal powder stream radius

where the denominator is the powder amount of the whole spot, and $\rho(r)$ is the gray value at r distance from the center point. In this study, the ratio p is set to be 0.7, and to obtain the R_p in radial direction, an iterative calculation is performed until p is greater than 0.7. During calculation, the initial value and increment of R_p are set as 0 and image pixel size, respectively. The distance between the minimum R_p position and the nozzle outlet is defined as the consolidation distance of the powder stream.

3 Results and discussion

3.1 Prediction of powder stream convergence

Figure 5 presents the computed particle trajectories during DED powder feeding process, which display a waist-like appearance. Given the symmetrical nature of the annular nozzle, only half of the geometry is considered in computations. The powder particles firstly enter the gap between the inner and outer nozzles from the top inlet, and then collide with the nozzle walls. These collisions cause the particles to be frequently reflected and redirected, making the particle trajectories below the nozzle outlet unpredictable based solely on the nozzle geometry. As the particles advance, they are accelerated by the drag force of the high-speed argon gas and gravity, resulting in a continuous momentum transfer. Upon ejection from the nozzle outlet, the powder stream begins to converge, and at a certain in-flight distance, a high-concentration powder cluster forms. Beyond this region, the powder stream starts to diverge. The particle
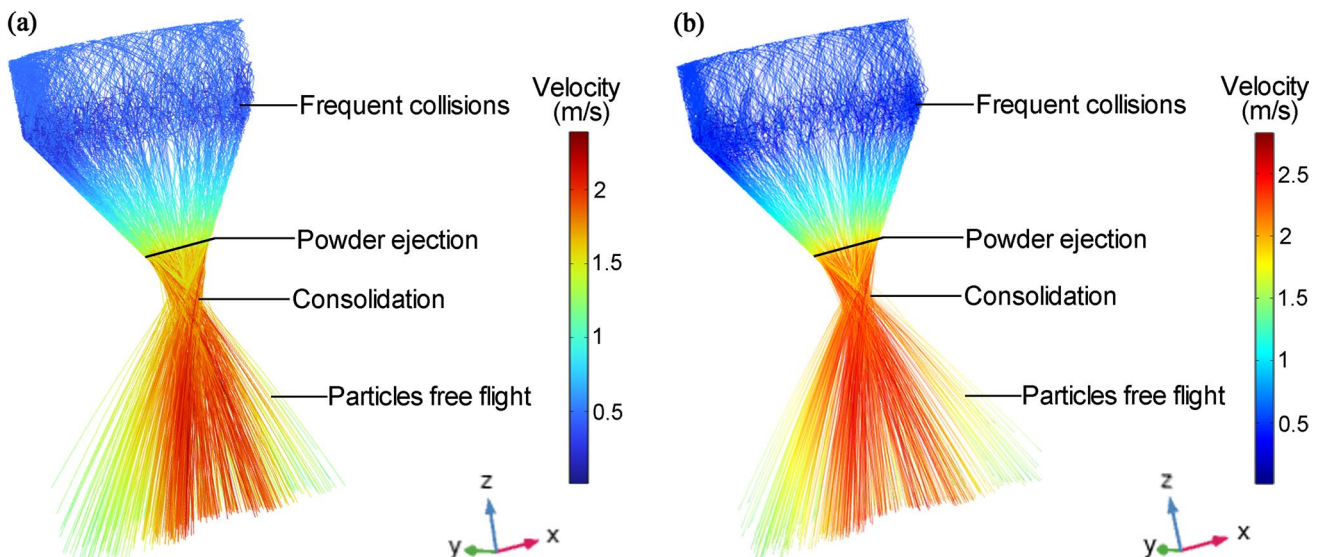

Fig. 5 Simulated particle trajectories colored by velocity with an inner gas flow rate of 15 L/min and different carrier gas flow rates: **a** 8 L/min, **b** 10 L/min

trajectories reveal a consistent distribution pattern at different gas flow rates. The maximum velocity of the powder particles increases from 2.39 to 2.82 m/s with increasing the carrier gas flow rate from 8 to 10 L/min. This indicates that the carrier gas serves as the primary driving force for the powder feeding process.

Figure 6 illustrates the particle concentration distribution at various XY cross-sections by using the method in Sect. 2.1.2. The cross-sectional distribution of powder concentrations aligns with the form of particle trajectories depicted in Fig. 5. The powder stream below the nozzle outlet can be categorized into three stages:

pre-convergence, convergence, and divergence. In the initial stage, the powder concentration distribution on the XY section presents a ring-like shape, with the ring radius continuously shrinking due to the confinement of the inner and outer nozzle walls. Consequently, the powder particles gravitate towards the convergence region upon exiting the nozzle. In the second stage, the powder flow commences converge at $z = -8$ mm and attains a peak concentration of 69.8 kg/m^3 at z of approximately -11 mm. The concentration of the powder stream aggregates at a single point, indicating the distinct characteristics of powder flow convergence, as shown in Fig. 6b. In the final stage, as the
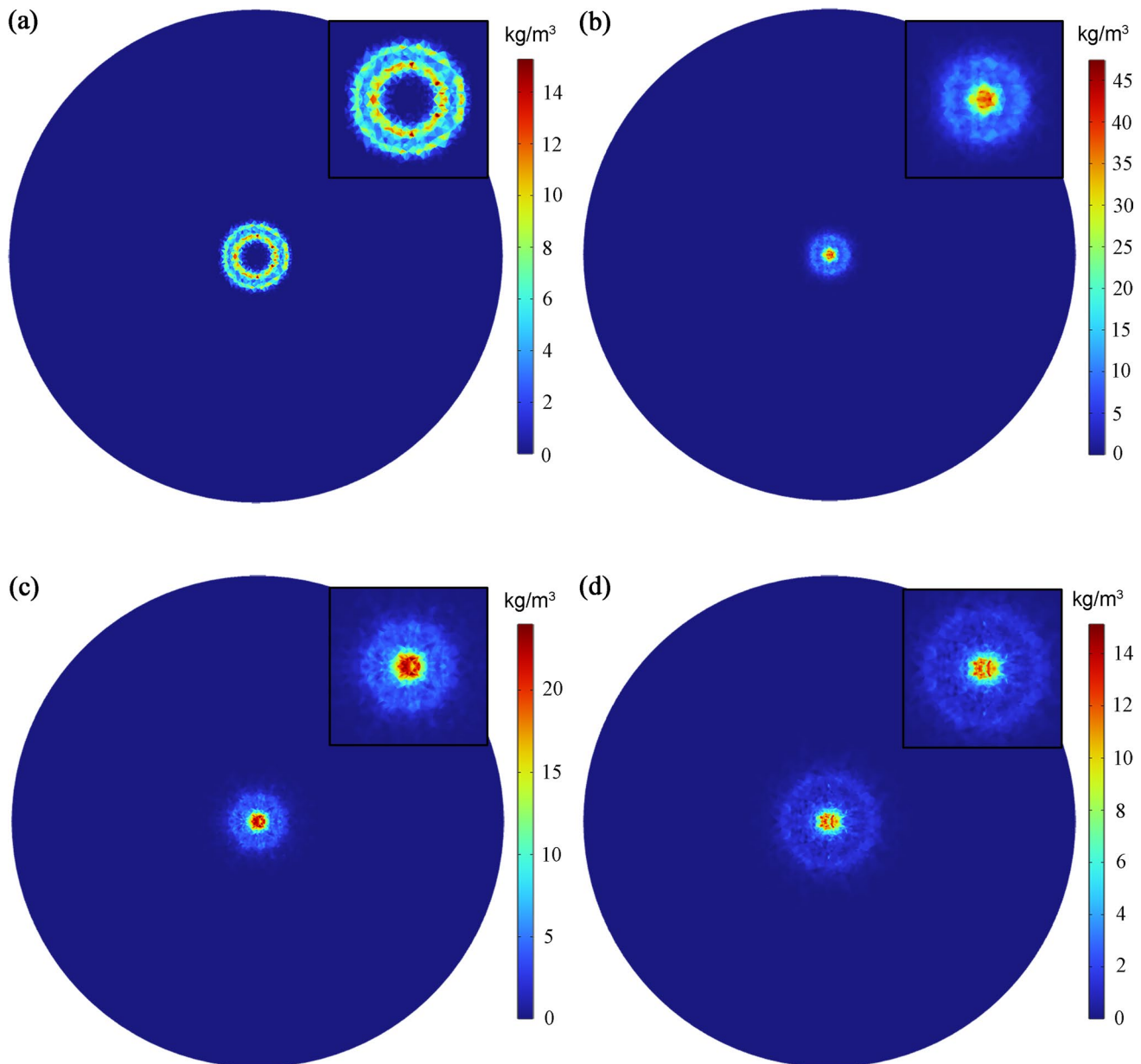

Fig. 6 Powder concentration distribution on different x–y cross sections: **a** $z = -5$ mm, **b** $z = -10$ mm, **c** $z = -15$ mm, and **d** $z = -20$ mm
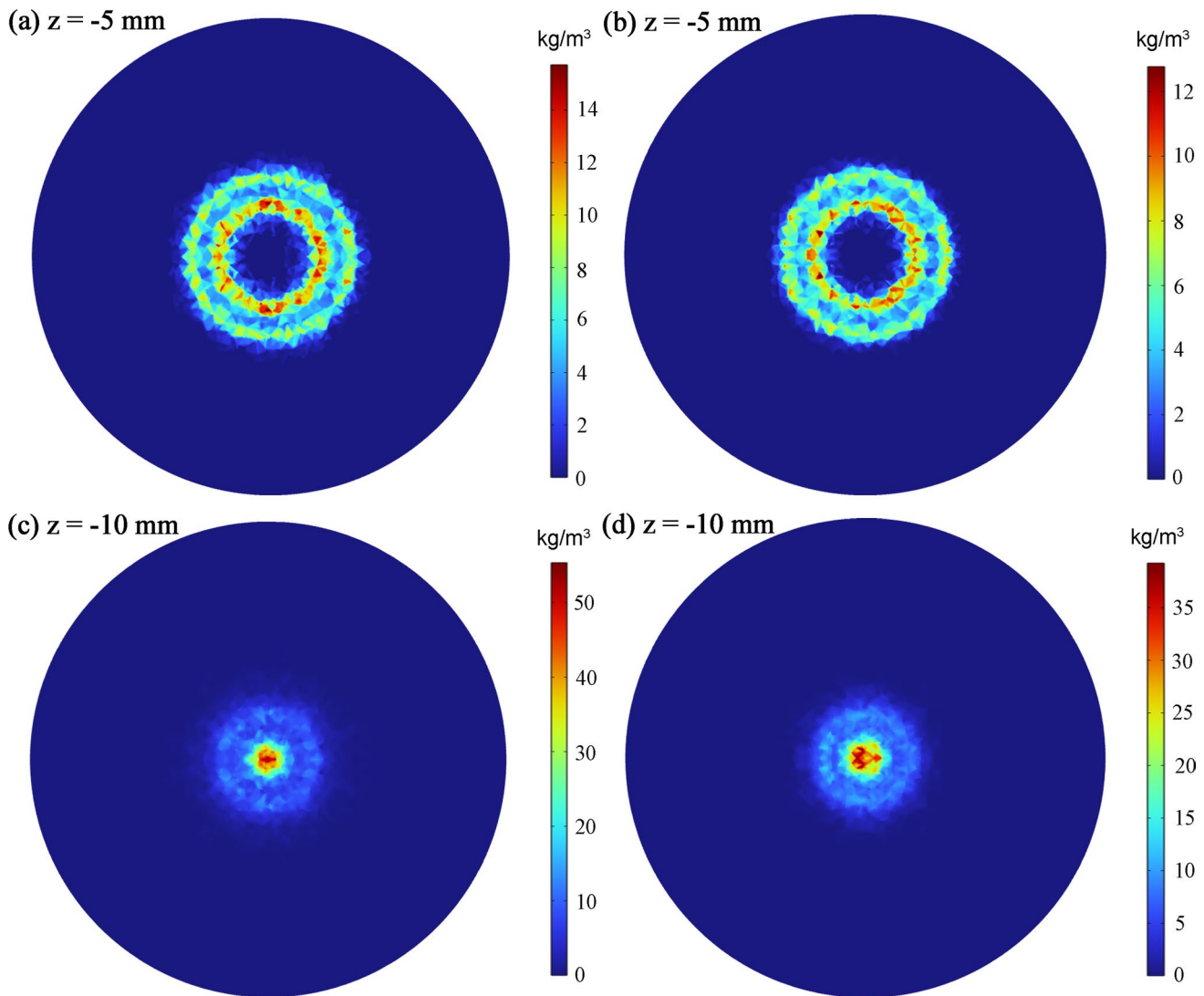
Fig. 7 Powder concentration distribution on different x–y cross sections at different carrier gas flow rates: **a**, **c** 8 L/min, **b**, **d** 10 L/min

powder flow progresses, the powder concentration swiftly reduces to around 14.3 kg/m^3. Figure 6d confirms that the apparent divergence of cross-sectional powder concentration appears at $z = -20$ mm.

The powder stream concentration distributions exhibit similar convergence and divergence stages across different carrier gas flow rates. As illustrated in Fig. 7, when the carrier gas flow rate increases from 8 to 12 L/min, the maximum powder concentration within the cross-section at an equivalent distance from the nozzle outlet diminishes, i.e., the maximum concentration of 15.73 kg/m^3 in Fig. 7a exceeds that of 12.78 kg/m^3 in Fig. 7b. This variance is significant between Fig. 7c and d. The increased carrier gas flow rates intensify the collision between the

powder particles and nozzle walls, resulting in a more uniform concentration distribution of the powder stream.

3.2 Prediction of powder stream thermal history

Figure 8 illustrates the trajectories of powder particles under two different laser powers, which are colored by the magnitude of temperature. These particles begin to enter the laser irradiation area at approximately 8 mm below the nozzle exit, as indicated by a significant elevation in the temperature. When they pass through the DOF of the laser beam, they are rapidly heated to high temperatures. As the particles continue to move forward, the heated particles disperse in a free space. As shown in Fig. 8b, the overall temperature of
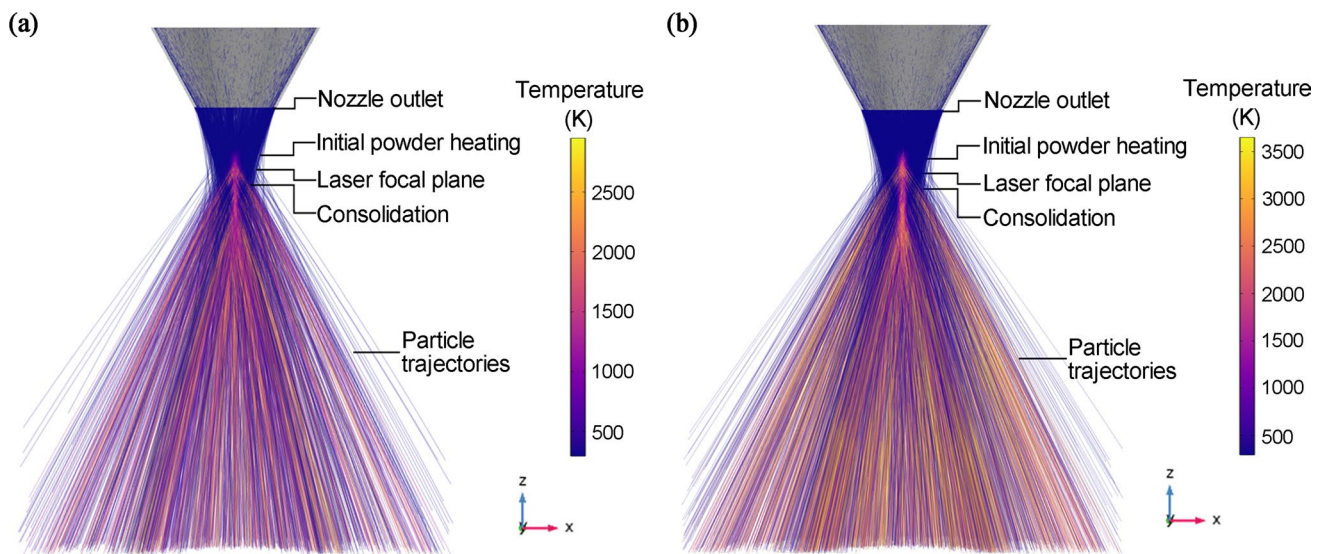
Fig. 8 Powder stream temperature distribution at different laser powers: **a** 800 W, **b** 1000 W
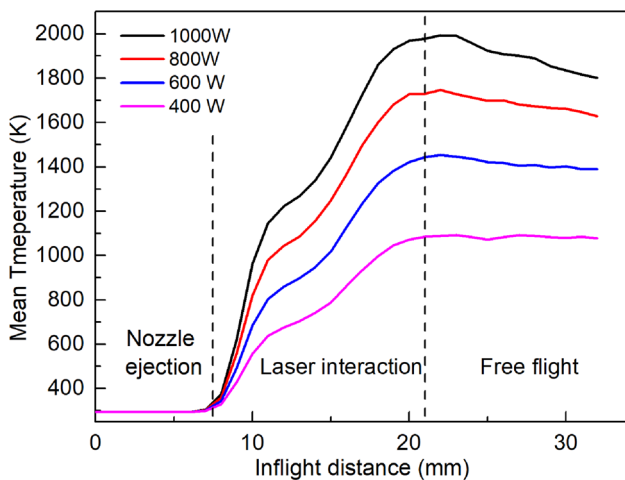

Fig. 9 The average temperature of the powder stream along the z-axis under different laser powers

the particle trajectories at a laser power of 1000 W is significantly higher than that at a laser power of 800 W presented in Fig. 8a. Under the same interaction duration within laser irradiation area, the laser intensity is significant for the laser heating effect. Figure 9 presents the variation curve of the average particle temperature along the z-axis under different laser powers. A large gradient in temperature is noticeable around the laser focal plane, followed by a gradual heating zone until the maximum temperature is achieved. Beyond this region, the particle temperature tends to be steady. It is evident that particles exhibit a similar thermal history trend across different laser powers, with a higher laser power leading to a higher maximum particle temperature.

To comprehensively understand the heating process involving multiple particles, temperature distributions with respect to the radial distance colored by particle velocities are presented in Fig. 10, where the particle temperature and velocity data are extracted from four different cross sections along z-axis. As depicted in Fig. 10a, the particles are located at the periphery of the laser beam and thus remain at room temperature. As the particles advance to the z of -10 mm, the particle temperature distribution presents a dromedary pattern, with the highest temperature at the center and a gradual decay along the radial direction, as shown in Fig. 10b. Notably, the particle temperature in the central area sharply rises to approximately 1300 K, which is a clear indication of the laser heating effect.

Owing to the divergence of the powder stream, a subset of particles is observed at positions that are distant from the z-axis, as shown in Fig. 10c. Some of these particles traverse the high laser intensity region, interacting with the laser beam for an extended duration. Therefore, their temperatures are higher than those of particles exposed to a shorter irradiation time in the low laser intensity region. This phenomenon is still present in Fig. 10d. Furthermore, a portion of particles undergoes melting phase transformation as their temperature exceeds the solidus temperature of 1528 K. The overall particle temperature continues to increase due to the intense laser irradiation, and the heated powder stream is in a state of complete divergence. The radial temperature distribution of the particles corresponds to the thermodynamics illustrated in Figs. 6 and 7. In terms of the radial distribution, the distribution of the powder stream significantly influences the thermal profile of the particles.
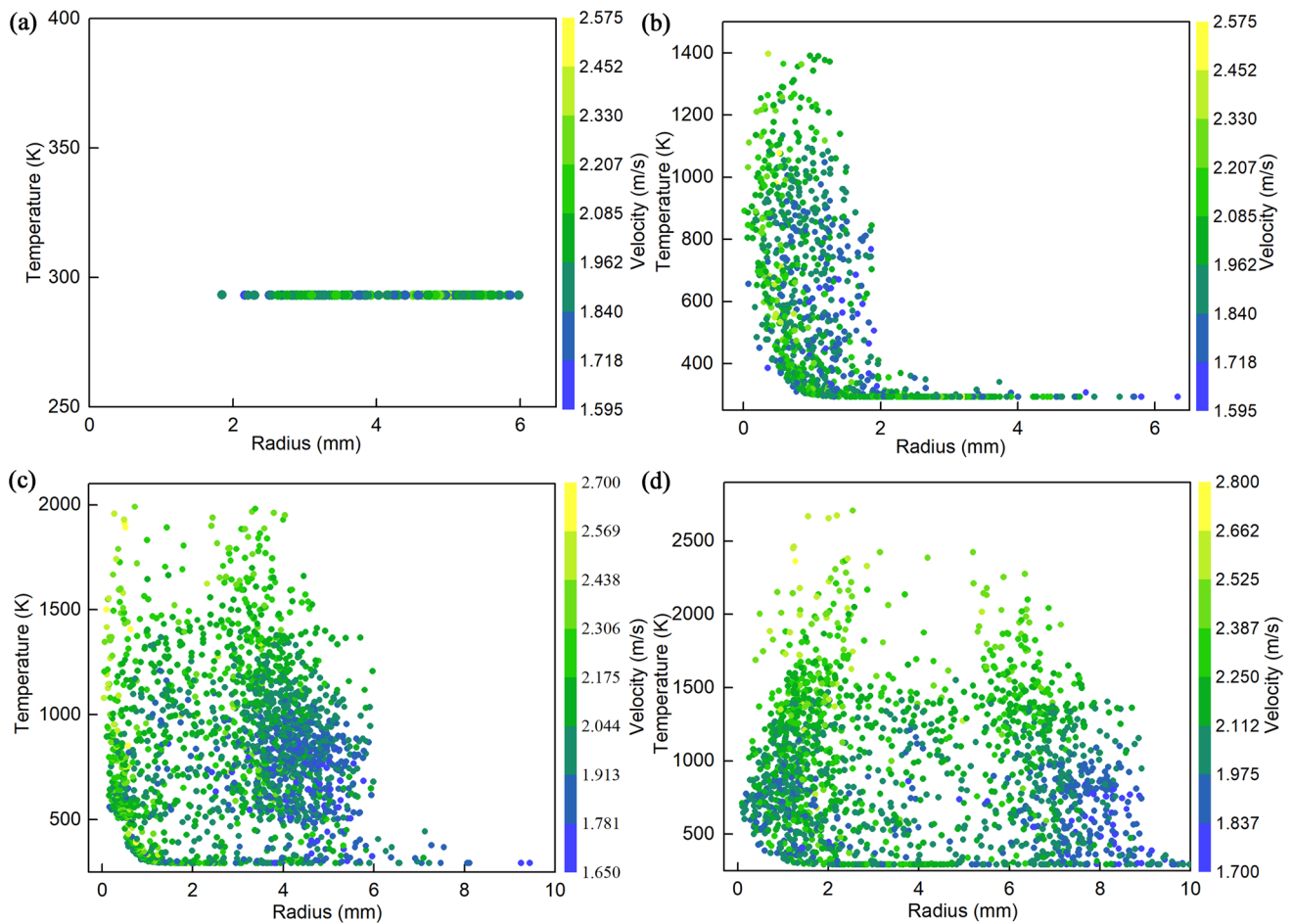
Fig. 10 Particle temperature scatters colored by velocity on different cross sections at a laser power of 800 W: **a** $z = -5$ mm, **b** $z = -10$ mm, **c** $z = -15$ mm, and **d** $z = -20$ mm

3.3 Effect of laser-powder offset on thermal efficiency

The discrepancy between the powder consolidation distance and the laser focal length significantly affects the thermal interaction between the powder stream and the laser beam. In this study, we flexibly adjusted this offset to investigate the DED powder heating efficiency that is commonly difficult to be determined experimentally. We define the powder heating efficiency as the proportion of particles heated to the melting temperature within a space of 0.5 mm in height and 1.5 mm in radius near the consolidation plane.

Figure 11 illustrates the variation of particle heating efficiency against offset. A negative offset indicates that the laser beam focuses ahead of the powder stream. With a negative offset, the powder particles have long interaction time with the laser beam before reaching the substrate, owing to the existence of the DOF. Conversely, at a positive offset, the laser beam has not yet begun to focus when the powder stream reaches the convergence region.
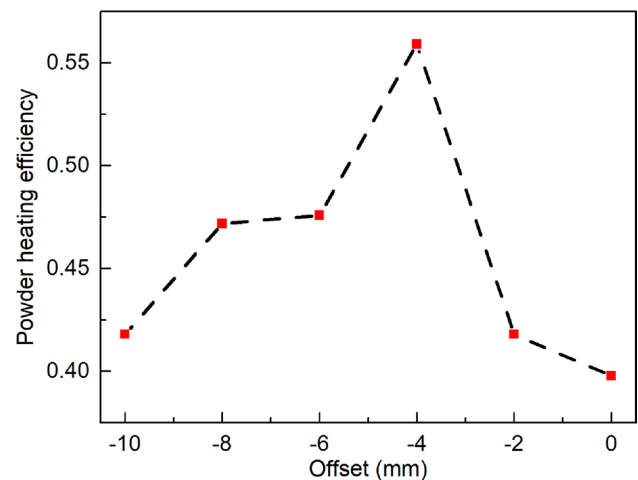

Fig. 11 Variations of powder heating efficiency against the offset between laser beam and powder stream

The maximum powder heating efficiency, 55.9%, appears at an offset of − 4 mm, demonstrating a significant improvement of 16.2% compared to the mode of simultaneous focusing. A better alignment between the powder consolidation distance and the laser beam can enhance the powder stream heating efficiency, thereby improving the powder capture efficiency.

3.4 Experimental determination of powder stream convergence

Figure 12a depicts the particles as white bright spots after the threshold segmentation binarization process. Upon exiting the nozzle, the particles have a mean velocity of 1.5 m/s and are further accelerated by trailing and gravitational forces to a maximum velocity of 2.8 m/s. These values are calculated based on the length of trajectories. In Fig. 12b, the averaged image is relatively smooth, and the powder concentration displays improved distribution characteristics compared to that in Fig. 12a. This suggests that the preprocessing operations of background correction and homogenization effectively mitigate the impacts of particle trajectory randomness. Figure 12c presents a contour plot of the powder concentration distribution, which clarifies the effective area of the powder stream. The highest powder concentration is observed at the consolidation position. Also, it is reasonable that the convergence of powder streams can be well described by the nominal powder size R_p.
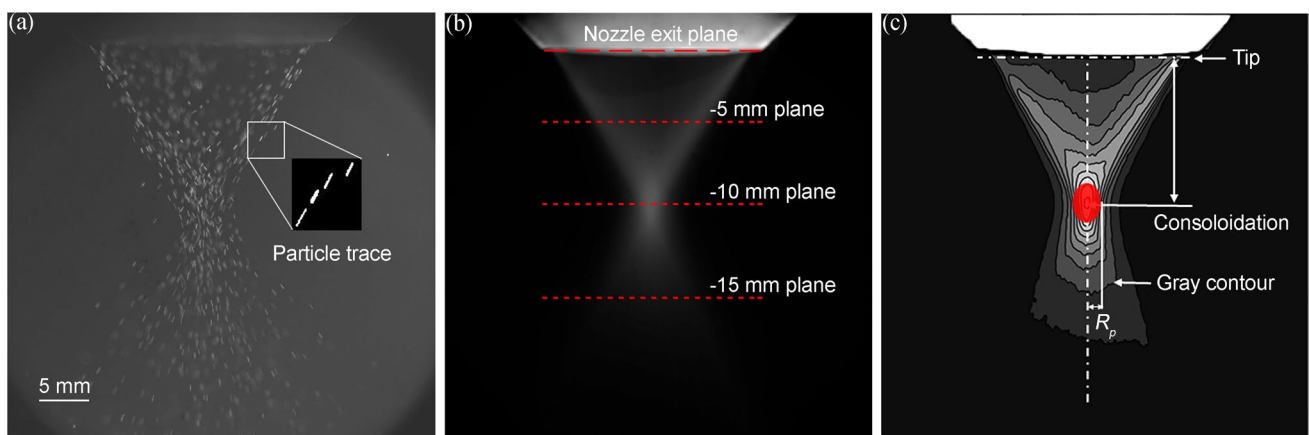

Fig. 12 Powder stream image preprocessing: **a** an original particle image, **b** an averaged particle image, and **c** the powder stream concentration contour
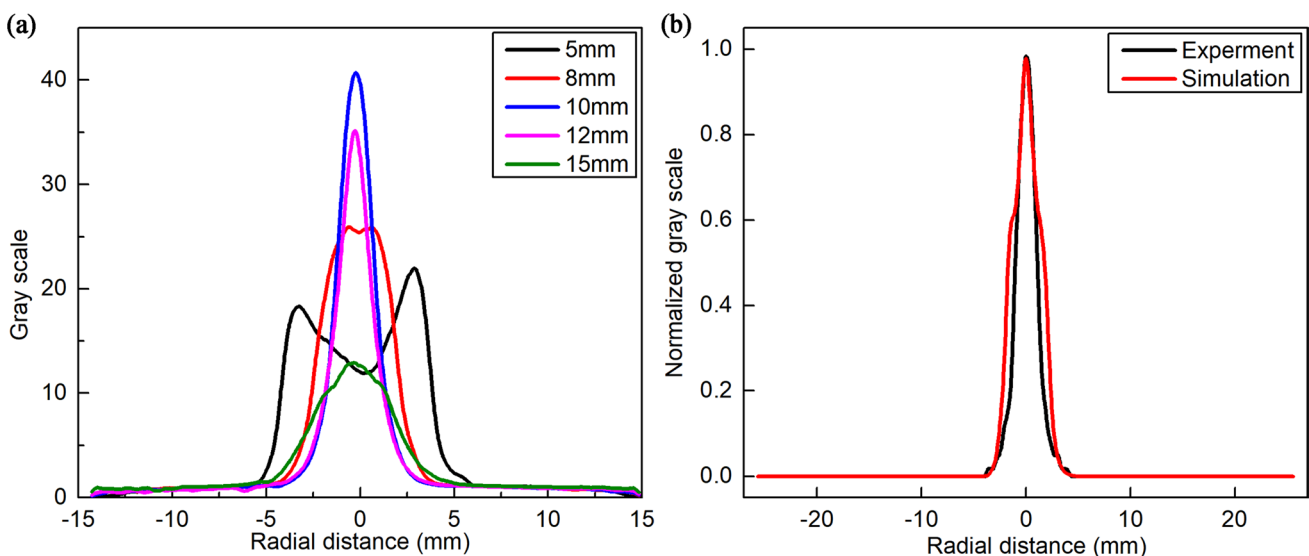

Fig. 13 Powder stream concentration profiles: **a** different distances below the nozzle exit and **b** normalized profile comparison at an in-flight distance of 10 mm

Given a carrier gas volume flow rate of 10 L/min and a shielding gas volume flow rate of 15 L/min, five profiles of the gray value at varying distances from the nozzle outlet are extracted to quantitatively illustrate the powder stream distribution. As shown in Fig. 13a, at a distance of 5 mm from the nozzle outlet, the powder concentration profile exhibits a bimodal shape with low gray values. As the in-flight distance increases, the distribution curve exhibits a peak with a high gray value, indicating that the powder particles gradually aggregate to a single point.

Obviously, the consolidation distance of the powder stream lies within the range of 10–12 mm below the nozzle exit. Beyond this region, the powder stream diverges, which will not contribute to the formation of the clad. As shown in Fig. 13b, the comparison of the normalized concentration profile reveals a good agreement between the experimental and simulated results.

3.5 Effect of gas flow rates on powder consolidation distance

The role of auxiliary gas in influencing the consolidation distance of the powder stream is significant. In this study, three different gas flow rates (8, 10, and 12 L/min) are selected to examine the interplay between the inner and carrier gas. The consolidation distances, both simulated and experimental, were determined using the method in Sect. 2.4.

Figure 14 illustrates the variation of the powder stream consolidation distance in relation to the inner and outer gas flow rates in the coaxial nozzle. As shown in Fig. 14a, an increase in the inner gas flow rate results in a further movement of approximately 0.2 mm the consolidation distance

from the nozzle outlet. This displacement helps to prevent the premature convergence of the powder flow due to the inner gas's blowing effect. On the other hand, an increase in the carrier gas flow rate, especially when it exceeds the inner gas flow rate, gradually reduces the consolidation distance of the powder stream, thereby enhancing the quality of powder stream convergence, as depicted in Fig. 14b. The minor discrepancy depicted in the figure remains within 5%, indicating a good agreement between the simulated and experimental results. The constant offset between the two is justifiable, considering that the simulation has not yet accounted for the energy loss from particle–wall collisions.

3.6 Comparison between the experimental and simulated data

The simulated results are validated by the experiment described in Sect. 2.3. As seen from Fig. 15a, both the experimental and simulated results demonstrate a fact that as the in-flight distance extends from 10 to 40 mm, the powder temperature increases from 1000 to 1800 K, and then decreases from 1800 to 1600 K. This pattern reflects the heating of the powder particles in the laser irradiation region, followed by a cooling stage where heat is dissipated through convection and radiation during free flight. The R^2 value of 0.96 for the average temperature prediction demonstrates a good agreement between the experimental and simulated data. Furthermore, Fig. 15b depicts a consistent increase in the mean velocity of the powder particles with the expansion of the in-flight distance. An R^2 value of 0.91 for the velocity prediction also indicates a good consistency of experimental and simulated results.
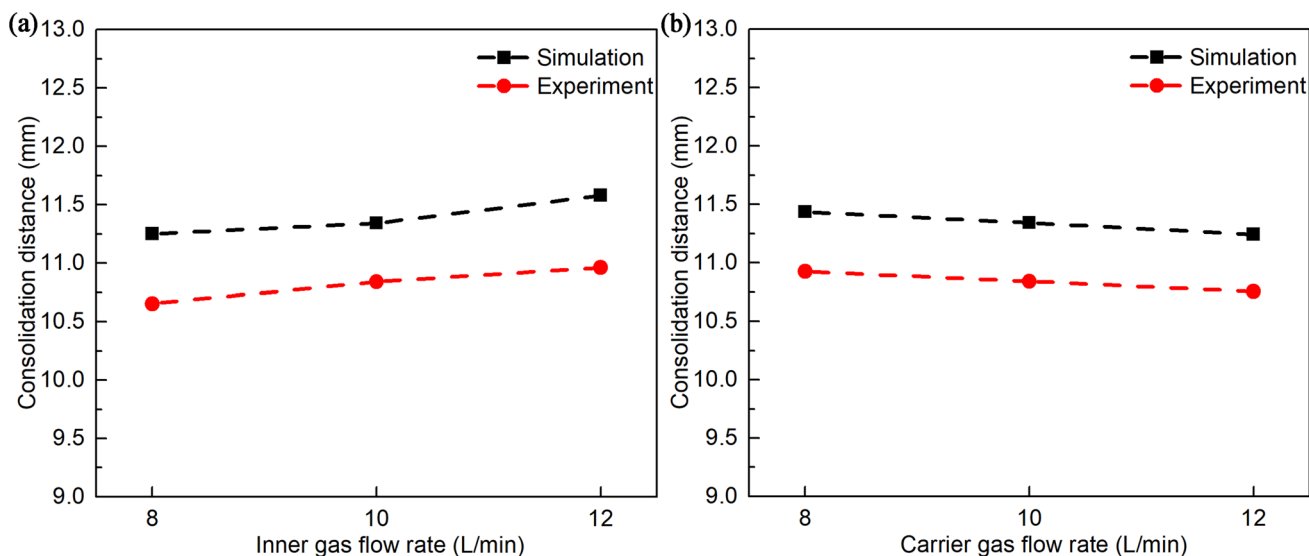

Fig. 14 Influences of gas flow rates on the powder stream consolidation distance: **a** a carrier gas flow rate of 10 L/min and **b** an inner gas flow rate of 10 L/min
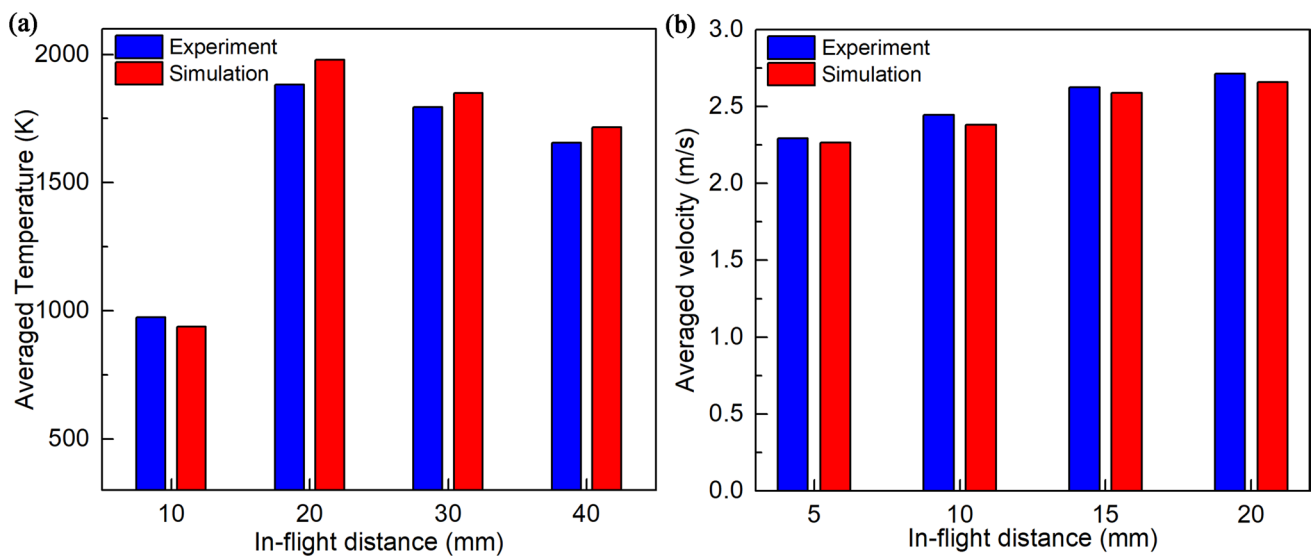
Fig. 15 Comparison between the experimental and simulated results: **a** averaged particle temperatures and **b** averaged particle velocities
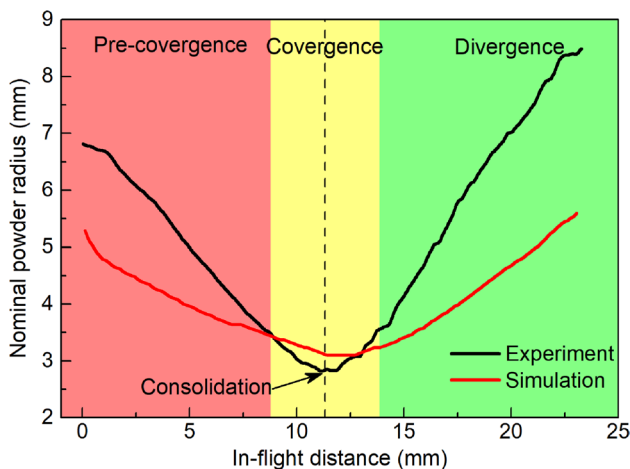

Fig. 16 Comparison of powder stream nominal radius (R_p, $p=0.7$) along z-axis

In addition, the method outlined in Sect. 2.4 was employed to assess the convergence of the powder stream. Figure 16 depicts the variation of the nominal radius (R_p) of the powder stream along the z-axis, with the two curves representing the experimental and simulated results. Initially, the powder stream has a large R_p value, which is indicative of a low powder concentration. As the in-flight distance expands, the R_p value gradually diminishes until reaching a minimum of 2.8 mm, implying the consolidation of the powder stream at approximately 11.2 mm. After this position, the R_p value increases due to the divergence of the powder stream. Both the simulated and experimental results display a U-shaped curve along the in-flight direction. This reveals the three stages of powder stream evolution, i.e., the

pre-convergence, convergence, and divergence. The comparison verifies a good agreement between the simulated and experimental results, particularly in the region of powder stream convergence. During the experiment, some particles situated in the defocused area of the camera were not captured, whereas the simulation accurately accounted for all particles. Thus, the difference of the R_p in pre-convergence and divergence region resents reasonably.

4 Conclusions

In this study, a 3D numerical model is developed to systematically explore the intricate interactions among the powder, gas, and laser beam. A quantitative analysis is conducted on the structure, movement, and heating behavior of the powder stream. The experimental observation based on image processing is also carried out to validate the model. The conclusions are summarized as follows:

1) The simulation results identify the three stages of the powder flow, i.e., pre-convergence, convergence, and divergence. The maximum powder concentration is found to be 68.9 kg/m^3, and the minimum R_p is 2.8 mm at an in-flight distance of 11.2 mm.

2) The average velocity and temperature of the powder stream at specific distances below the nozzle outlet have a good agreement between the experimental and simulated results, with R^2 values of 0.91 and 0.96, respectively.

3) The gas flow rate has a certain effect on the powder stream convergence. The carrier gas facilitates better consolidation of the powder stream, whereas the blowing

effect of the inner gas tends to shift the consolidation distance away from the nozzle outlet.

4) The simulation reveals that a laser heating efficiency of 55.9% could be achieved when the laser beam is focused at 4 mm ahead of the powder stream. The efficiency is significantly improved of 16.2% compared to the case of zero offset.

This study provides an effective approach to comprehend and improve the convergence and heating efficiency of the DED powder feeding process by numerical simulation. In the future, the current model's capabilities of accurate predictions of the powder velocity and temperature will be utilized as inputs to further investigate the thermodynamic effects of particles on the molten pool.

Author contribution Xiaoguang Qu: methodology, software, formal analysis, data curation, writing—original draft. Ze Chai: conceptualization, writing—review and editing, supervision. Tongtong Liu: resources, visualization. Huabin Chen: investigation, visualization. Xiaoqi Chen: funding acquisition, writing—review and editing, supervision.

Data availability The data that support the findings of this study are available from the corresponding author upon reasonable request.

Declarations

Ethical approval Not applicable.

Consent to participate The manuscript has been read and approved by all authors.

Competing interests The authors declare no competing interests.

References

1. Gao W, Zhang Y, Ramanujan D, Ramani K, Chen Y, Williams CB, Wang CC, Shin YC, Zhang S, Zavattieri PD (2015) The status, challenges, and future of additive manufacturing in engineering. Comput -Aided Des 69:65–89. https://doi.org/10.1016/j.cad.2015.04.001
2. Schmidt M, Merklein M, Bourell D, Dimitrov D, Hausotte T, Wegener K, Overmeyer L, Vollertsen F, Levy GN (2017) GN laser based additive manufacturing in industry and academia. CIRP Ann 66:561–583. https://doi.org/10.1016/j.cirp.2017.05.011
3. Galantucci LM, Guerra MG, Dassisti M, Lavecchia F (2019) Additive manufacturing: new trends in the 4th industrial revolution. In: Proceedings of the 4th International Conference on the Industry 4.0 Model for Advanced Manufacturing, Springer International Publishing AG, Switzerland, pp 153–169. https://doi.org/10.1007/978-3-030-18180-2_12
4. Ahn DG (2021) Directed energy deposition (DED) process: state of the art. Int J of Precis Eng Manuf Green Tech 8:703–742. https://doi.org/10.1007/s40684-020-00302-7
5. Renjith SC, Park K, Okudan Kremer GE (2020) A design framework for additive manufacturing: integration of additive manufacturing capabilities in the early design process. Int J Precis Eng Manuf 21:329–345. https://doi.org/10.1007/s12541-019-00253-3
6. Laser metal deposition (LMD). (2023) https://www.trumpf.com/en_SG/solutions/applications/additive-manufacturing/laser-metal-deposition/. Accessed 7 October 2023
7. Schopphoven T, Gasser A, Backes G (2017) EHLA: extreme high-speed laser material deposition economical and effective protection against corrosion and wear. Laser Tech J 4:26–29. https://doi.org/10.1002/latj.201700020
8. Sames WJ, List FA, Pannala S, Dehoff RR, Babu SS (2016) The metallurgy and processing science of metal additive manufacturing. Int Mater Rev 61:315–360. https://doi.org/10.1080/09506608.2015.1116649
9. Attaran M (2017) The rise of 3-D printing: the advantages of additive manufacturing over traditional manufacturing. Bus Horiz 60:677–688. https://doi.org/10.1016/j.bushor.2017.05.011
10. Niaki MK, Torabi SA, Nonino F (2019) Why manufacturers adopt additive manufacturing technologies: the role of sustainability. J Cleaner prod 222:381–392. https://doi.org/10.1016/j.jclepro.2019.03.019
11. Korinko P, Adams TM, Malene SH, Gill D, Smugeresky J (2011) Laser engineered net shaping® for repair and hydrogen compatibility. Weld J 90:171–181
12. Costa L, Vilar R (2009) Laser powder deposition. Rapid Prototyp J 15:264–279. https://doi.org/10.1108/13552540910979785
13. Gu D, Xia M, Dai D (2019) On the role of powder flow behavior in fluid thermodynamics and laser processability of Ni-based composites by selective laser melting. Int J Mach Tool Manufact 137:67–78. https://doi.org/10.1016/j.ijmachtools.2018.10.006
14. Chen H, Wei Q, Wen S, Li Z, Shi S (2017) Flow behavior of powder particles in layering process of selective laser melting: numerical modeling and experimental verification based on discrete element method. Int J Mach Tool Manufact 123:146–159. https://doi.org/10.1016/j.ijmachtools.2017.08.004
15. Mouchard A, Pomeroy M, Robinson J, McAuliffe B, Donovan S, Tanner D (2021) An analytical method for powder flow characterization in direct energy deposition. Addit Manuf 42:101991. https://doi.org/10.1016/j.addma.2021.101991
16. Liu Z, Zhang HC, Peng S, Kim H, Du D, Cong W (2019) Analytical modeling and experimental validation of powder stream distribution during direct energy deposition. Addit Manuf 30:100848. https://doi.org/10.1016/j.addma.2019.100848
17. Pinkerton AJ, Li L (2004) Modelling powder concentration distribution from a coaxial deposition nozzle for laser-based rapid tooling. J Manuf Sci Eng 126:33. https://doi.org/10.1115/1.1643748
18. Pinkerton AJ, Li L (2002) A verified model of the behaviour of the axial powder stream concentration from a coaxial laser cladding nozzle. International Congress on Applications of Lasers & Electro-Optics 165528, AIP Publishing, Orlando. https://doi.org/10.2351/1.5066174
19. Tan H, Fang Y, Zhong C, Yuan Z, Fan W, Li Z, Lin X (2020) Investigation of heating behavior of laser beam on powder stream in directed energy deposition. Surf Coat Technol 397:126061. https://doi.org/10.1016/j.surfcoat.2020.126061
20. Jhang SS, Lo YL, Le TN (2019) Systematic modeling approach for analyzing the powder flow and powder energy absorptivity in direct energy deposition system. Int J Adv Manuf Technol 105:1765–1776. https://doi.org/10.1007/s00170-019-04441-3
21. Gao X, Yao XX, Niu FY, Zhang Z (2022) The influence of nozzle geometry on powder flow behaviors in directed energy deposition additive manufacturing. Adv Powder Technol 33:103487. https://doi.org/10.1016/j.apt.2022.103487

22. Pacheco JT, Cardoso EL (2022) Simulation of the thermomechanical behavior of discrete particles in the laser directed energy deposition process. Powder Technol 405:117568. https://doi.org/10.1016/j.powtec.2022.117568

23. Zhang A, Li D, Zhou Z, Zhu G, Lu B (2010) Numerical simulation of powder flow field on coaxial powder nozzle in laser metal direct manufacturing. Int J Adv Manuf Technol 49:853–859. https://doi.org/10.1007/s00170-010-2657-8

24. Wen SY, Shin YC, Murthy JY, Sojka PE (2009) Modeling of coaxial powder flow for the laser direct deposition process. Int J Heat Mass Transfer 52:5867–5877. https://doi.org/10.1016/j.ijheatmasstransfer.2009.07.018

25. Guan X, Zhao YF (2020) Numerical modeling of coaxial powder stream in laser-powder-based directed energy deposition process. Addit Manuf 34:101226. https://doi.org/10.1016/j.addma.2020.101226

26. Tabernero I, Lamikiz A, Ukar E et al (2010) Numerical simulation and experimental validation of powder flux distribution in coaxial laser cladding. J Mater Process Technol 210:2125–2134. https://doi.org/10.1016/j.jmatprotec.2010.07.036

27. Mazzucato F, Tusacciu S, Lai M, Biamino S, Lombardi M, Valente A (2017) Monitoring approach to evaluate the performances of a new deposition nozzle solution for DED systems. Technologies 5:29. https://doi.org/10.3390/technologies5020029

28. Pant P, Chatterjee D, Samanta SK, Lohar AK (2021) Experimental and numerical analysis of the powder flow in a multi-channel coaxial nozzle of a direct metal deposition system. J Manuf Sci Eng 143:071003. https://doi.org/10.1115/1.4049640

29. Gouesbet G, Berlemont A (1999) Eulerian and Lagrangian approaches for predicting the behaviour of discrete particles in turbulent flows. Prog Energy Combust Sci 25:133–159. https://doi.org/10.1016/S0360-1285(98)00018-5

30. Bailly C, Comte-Bellot G (2015) Turbulence. Springer

31. Wilcox DC (1998) Turbulence modeling for CFD, DCW Industries, La Canada, pp 124–127

32. Stockholm, Sweden, COMSOL Multiphysics® v. 6.0, www.comsol.com

33. Chai Q, He X, Xing Y, Sun G (2023) Numerical study on the collision effect of particles in the gas-powder flow by coaxial nozzles for laser cladding. Opt Laser Technol 163:109449. https://doi.org/10.1016/j.optlastec.2023.109449

34. Haider A, Levenspiel O (1989) Drag coefficient and terminal velocity of spherical and non-spherical particles. Powder Technol 58:63–70. https://doi.org/10.1016/0032-5910(89)80008-7

35. Tian L, Ahmadi G (2007) Particle deposition in turbulent duct flows–comparisons of different model predictions. Aerosol Sci 38:377–397. https://doi.org/10.1016/j.jaerosci.2006.12.003

36. Zhao B, Yang C, Yang X, Liu S (2008) Particle dispersion and deposition in ventilated rooms: testing and evaluation of different Eulerian and Lagrangian models. Build and Environ 43:388–397. https://doi.org/10.1016/j.buildenv.2007.01.005

37. Ranz WE, Marshall WR (1952) Evaporation from drops, part I, Chem. Eng. Prog., American, pp 141–146

38. Hulst HC, van de Hulst HC (1981) Light scattering by small particles, Dover Publications, New York